JACS Au
AN OPEN ACCESS JOURNAL OF THE AMERICAN CHEMICAL SOCIETY

pubs.acs.org/jacsau

Article

Excited-State Intramolecular Hydrogen Transfer of Compact Molecules Controls Amyloid Aggregation Profiles

Mannkyu Hong,[‖] Mingeun Kim,[‖] Jiwon Yoon, Seung-Hee Lee,* Mu-Hyun Baik,* and Mi Hee Lim*

Cite This: *JACS Au* 2022, 2, 2001−2012

Read Online

ACCESS | Metrics & More | Article Recommendations | Supporting Information

ABSTRACT: Developing chemical methodologies to directly modify harmful biomolecules affords the mitigation of their toxicity by persistent changes in their properties and structures. Here we report compact photosensitizers composed of the anthraquinone (**AQ**) backbone that undergo excited-state intramolecular hydrogen transfer, effectively oxidize amyloidogenic peptides, and, subsequently, alter their aggregation pathways. Density functional theory calculations showed that the appropriate position of the hydroxyl groups in the **AQ** backbone and the consequent intramolecular hydrogen transfer can facilitate the energy transfer to triplet oxygen. Biochemical and biophysical investigations confirmed that these photoactive chemical reagents can oxidatively vary both metal-free amyloid-β (Aβ) and metal-bound Aβ, thereby redirecting their on-pathway aggregation into off-pathway as well as disassembling their preformed aggregates. Moreover, the in vivo histochemical analysis of Aβ species produced upon photoactivation of the most promising candidate demonstrated that they do not aggregate into oligomeric or fibrillar aggregates in the brain. Overall, our combined computational and experimental studies validate a light-based approach for designing small molecules, with minimum structural complexity, as chemical reagents targeting and controlling amyloidogenic peptides associated with neurodegenerative disorders.

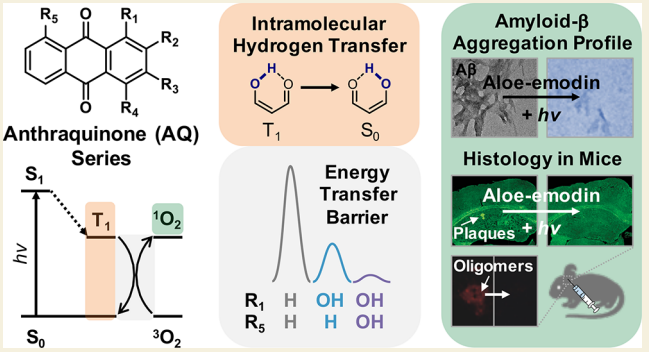

KEYWORDS: *photosensitizers, small molecules, ESIHT, amyloid-β, peptide aggregation*

INTRODUCTION

Modifications of peptides or proteins in nature lead to diverse structural frameworks that allow unprecedented activities, folding, location, and interactions.[1−5] Chemical methodologies to tactically manipulate certain amino acid residues installed in disease-related peptides or proteins have been developed for controlling the reactivities of these toxic biomolecules.[6] Structural variations on amyloid-β (Aβ) peptides have recently been recognized to be effective for altering their aggregation pathways that are linked to the pathology of Alzheimer's disease (AD).[7] These approaches include oxidation, covalent bond formation, and hydrolytic cleavage that offer permanent changes in peptides with minimum probability to aggregate into toxic forms.[8−11] In particular, the oxidative modifications of Aβ peptides with photosensitizers[12] or redox-active molecules[13−18] are the simplest strategy to change their aggregation profiles and improve cognitive defects in AD transgenic mice. A variety of photosensitizers ranging from fullerence or porphyrin -based macromolecules,[19,20] organometallic complexes,[21−26] nanoparticles,[27,28] and organic molecules[29−34] were designed to modulate the aggregation of Aβ. Despite their noticeable potential, the complexity of synthesis, the low blood−brain barrier (BBB) permeability,[35,36] and the potential risk of toxicity[37−39] remain significant hurdles to overcome. In addition, the dysregulation of metal ions [e.g., Fe(II/III), Cu(I/II), and Zn(II)] induces biologically detrimental outcomes.[40,41] Especially in the brains of AD patients, high concentrations of these metal ions are found in senile plaques, which implies that they could be a critical factor in the pathology of AD.[42] According to extensive studies, metal ions could bind to Aβ to form metal-bound Aβ (metal−Aβ) and, subsequently, influence the aggregation pathways of Aβ.[7,43,44] Indeed, the aggregation kinetics and morphology of Aβ species are significantly dependent on the concentration and type of metal ions. For example, the increased ratio of Cu(II) for Aβ could induce a shift from fibrillar structures to amorphous and spherical aggregates.[7,44] In the case of Zn(II), nonfibrillar assemblies could be produced and stabilized.[7,44]

We questioned if small organic photosensitizers carrying simple functionalities such as hydroxyl and carboxyl groups can

Received: May 8, 2022
Revised: July 11, 2022
Accepted: July 27, 2022
Published: August 11, 2022

https://doi.org/10.1021/jacsau.2c00281
JACS Au 2022, 2, 2001−2012

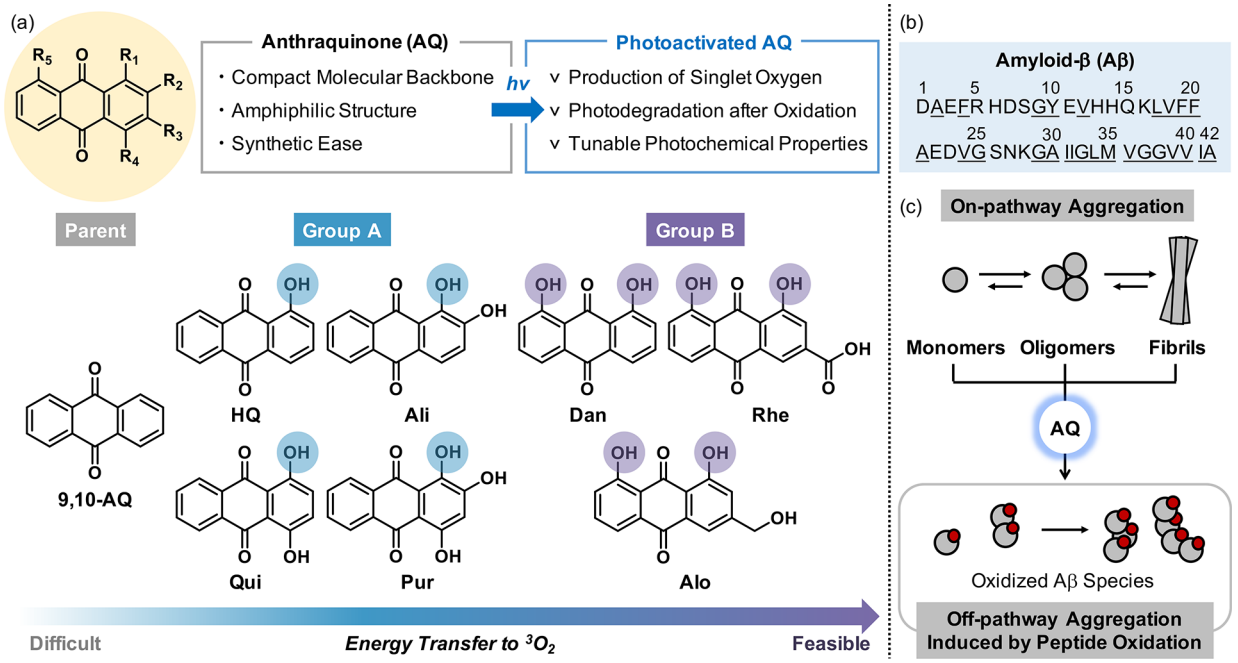

Figure 1. Rational selection of compact molecules that can modify the aggregation of Aβ with photoactivation. (a) Chemical structures and properties of **9,10-AQ** (**Parent**); **HQ**, **Ali**, **Qui**, **Pur** (**Group A**); **Dan**, **Rhe**, **Alo** (**Group B**). **9,10-AQ**, anthracene-9,10-dione; **HQ**, 1-hydroxyanthracene-9,10-dione; **Ali** (alizarin), 1,2-dihydroxyanthracene-9,10-dione; **Qui** (quinizarin), 1,4-dihydroxyanthracene-9,10-dione; **Pur** (purpurin), 1,2,4-trihydroxyanthracene-9,10-dione; **Dan** (dantron), 1,8-dihydroxyanthracene-9,10-dione; **Rhe** (rhein), 4,5-dihydroxy-9,10-dioxo-9,10-dihydroanthracene-2-carboxylic acid; **Alo** (aloe-emodin), 1,8-dihydroxy-3-(hydroxymethyl)anthracene-9,10-dione. (b) Sequence of Aβ. Hydrophobic residues are underlined. (c) Schematic description of the on-pathway aggregation of Aβ with the modulatory strategy employing the photoactivated **AQ** series.

oxidatively modify both metal-free Aβ and metal−Aβ and alter their aggregation profiles. Small molecule-based biosensors or probes have been reported to have notable sensibility against peptides[45] or other biomolecules.[46] As shown in Figure 1a, we rationally selected a series of anthraquinone (**AQ**)-based compounds and tested their capacity to oxidize metal-free Aβ and metal−Aβ upon photoirradiation and, consequently, vary their aggregation. In addition, the detailed mechanism for such reactivity was determined. Moreover, the aggregation behaviors of Aβ species produced upon light activation of the most promising molecule were probed in vivo. Collectively, our studies demonstrate that compact molecules with proper structural and photophysical features can be developed for manipulating Aβ aggregation with light.

RESULTS AND DISCUSSION

AQ-based dyes have been used as photosensitizers for various applications such as photovoltaics,[47] photocatalysts,[48−50] photoactive peptides,[51] and cell imaging;[52] thus, we chose the **AQ** backbone to identify effective photosensitizers that can oxidatively modify Aβ peptides. As displayed in Figure 1a, a series of **AQ**-based molecules with simple structural variations composed of only three basic carbon, hydrogen, and oxygen atoms were selected for this work. Based on the parent structure **9,10-AQ**, the hydroxyanthraquinone derivatives were classified into two groups: **Group A** (**HQ**, **Ali**, **Qui**, and **Pur**) possesses a hydroxyl group on the R_1 position forming one quasi-ring with the adjacent ketone and additional hydroxyl groups on R_2, R_4, or both; **Group B** (**Dan**, **Rhe**, and **Alo**) contains hydroxyl groups on both R_1 and R_5 generating two quasi-rings and structural variance on R_3. The anthraquinone skeleton and the aforementioned structural variation can offer several advantages in targeting Aβ. The **AQ** series has amphiphilic structures that can interact with Aβ consisting of both hydrophilic and hydrophobic amino acid residues, as visualized in Figure 1b. The addition of hydroxyl and carbonyl groups with the ketone functionality can provide additional binding sites with Aβ through hydrogen bonds. The π-plane backbone is not only essential for the photosensitizing ability but also enables hydrophobic interactions with the β-sheet in oligomeric and fibrillar Aβ.[53] As illustrated above, amphiphilicity has been known to be one of the essential assets for molecules to interact with proteins[54] or peptides.[55] Moreover, hydroxyl groups and the neighboring ketone functionality are envisioned to serve as potential metal-binding sites that can interact with other metal ions bound to Aβ. Upon photoactivation, anthraquinones are reported to generate singlet oxygen ($^1O_2$), which are highly reactive toward diverse biological substrates.[56,57] As such, we anticipated that **AQ** derivatives could readily oxidize amino acid residues in Aβ, as depicted in Figure 1c. We evaluated the $^1O_2$ production of compact molecules in the **AQ** series with mechanistic investigations and their reactivities toward both metal-free Aβ and metal−Aβ.

$^1O_2$ Production

The photochemical properties of the **AQ** series used in this study were examined by ultraviolet−visible (UV−Vis) and fluorescence spectroscopies. As summarized in Figure S1, the absorption spectra of the **AQ** series in dimethyl sulfoxide (DMSO) or the buffered solution showed maxima in the range of 326−486 and 335−516 nm, respectively, denoting photon absorbance in the blue light region. In particular, the absorption of **Ali** and **Pur** in the buffered solution displayed bathochromic shifts (λ = 82 and 21 nm, respectively) relative

https://doi.org/10.1021/jacsau.2c00281
JACS Au 2022, 2, 2001−2012

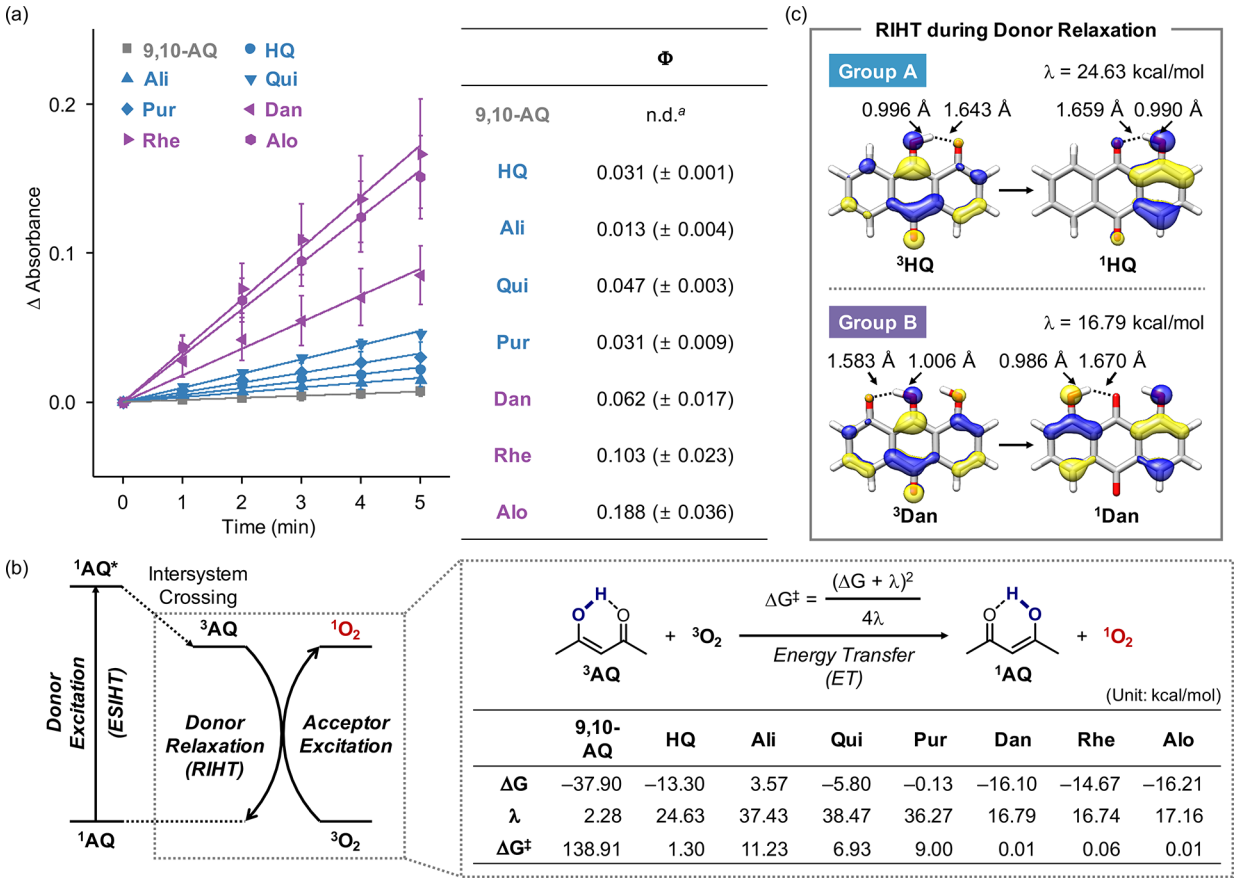

	Φ
9,10-AQ	n.d.[a]
HQ	0.031 (± 0.001)
Ali	0.013 (± 0.004)
Qui	0.047 (± 0.003)
Pur	0.031 (± 0.009)
Dan	0.062 (± 0.017)
Rhe	0.103 (± 0.023)
Alo	0.188 (± 0.036)

	9,10-AQ	HQ	Ali	Qui	Pur	Dan	Rhe	Alo
ΔG	−37.90	−13.30	3.57	−5.80	−0.13	−16.10	−14.67	−16.21
λ	2.28	24.63	37.43	38.47	36.27	16.79	16.74	17.16
ΔG‡	138.91	1.30	11.23	6.93	9.00	0.01	0.06	0.01

Figure 2. Production of $^1O_2$ by the **AQ** series upon photoactivation. (a) Amount of $^1O_2$ generated by the **AQ** series with light exposure analyzed by the ABDA assay and their quantum yields (Φ). Error bars represent the standard error of the mean from three independent experiments. (b) DFT-calculated energy transfer barriers ($\Delta G^{\ddagger}$) and their components (ΔG, singlet−triplet free energy gap; λ, reorganization energy) for each compound. (c) Structural comparison between **HQ** (**Group A**) and **Dan** (**Group B**) and key intramolecular hydrogen transfer that determines the different reorganization energy. Conditions: [compound] = 25 μM; [ABDA] = 100 μM; room temperature; Kessil lamp (467 nm) for 0, 1, 2, 3, 4, and 5 min. [a]n.d., not determined due to the limited production of $^1O_2$.

to the maximum in DMSO because the hydroxyl group at the R_2 position is deprotonated at neutral pH.[58] Moreover, the luminescence spectra of the **AQ** series in DMSO and the buffered solution were measured, as presented in Figure S2. While **9,10-AQ** had a maximum emission wavelength at 425 nm in DMSO and diminished absorbance in the buffered solution, the rest of the **AQ** series emitted light within the range of 554−612 nm upon illumination. Luminescence of **Ali** and **Pur** was not observed in the buffered solution.

The capability of the **AQ** series to produce $^1O_2$ in the wavelength of the blue light spectrum (ca. 467 nm) was evaluated employing the ABDA assay [ABDA = 9,10-anthracenediyl-bis(methylene)dimalonic acid]. As illustrated in Figures 2a and S3, the absorbance attenuation (ΔA) of ABDA in the presence of the **AQ** series under aerobic conditions revealed the energy transfer from the compounds in **Group B** toward O_2 exhibiting a range of Φ from 0.062 up to 0.188 comparable to $[Ru(bpy)_3]^{2+}$ (Φ = 0.18 in H_2O)[59−61] as a reference molecule. $[Ru(bpy)_3]^{2+}$ was reported to oxidize Aβ species, resulting in inhibiting the self-aggregation of Aβ and dismantling Aβ aggregates under illumination.[62] The molecules in **Group A** displayed moderate or low $^1O_2$ formation with a Φ range from 0.013 to 0.047. Note that the Φ value of **9,10-AQ** could not be obtained due to the minimum changes of the absorption peaks of ABDA. Therefore, the photochemical measurements confirm that the **AQ** series generates $^1O_2$ and the molecules in **Group B** are most effective.

Mechanism for $^1O_2$ Generation

Density functional theory (DFT) calculations were performed to estimate the ability of our selected molecules to produce $^1O_2$ upon photoirradiation. As illustrated in Figure 2b, the energy transfer occurs from the triplet excited photosensitizer (^{3}**AQ**) to the acceptor triplet oxygen ($^3O_2$) resulting in a singlet ground state photosensitizer (^{1}**AQ**) and a singlet excited state acceptor ($^1O_2$).[63] Hydroxyanthraquinones exhibit excited-state intramolecular hydrogen transfer (ESIHT) from hydroxyl groups toward the adjacent ketone functionality during light activation.[64] Moreover, hydroxyanthraquinones with deuterium-substituted hydroxyl groups are reported to have longer emission lifetimes, compared to nonsubstituted analogues.[65] Through notable isotope effects on the emission decay time, it has been proposed that the O−H vibration of hydroxyl groups is strongly coupled with the relaxation process.[66] Therefore, we can hypothesize that the donor relaxation could be also linked to the reverse intramolecular hydrogen transfer (RIHT) process. The relationship between the energy transfer and RIHT was investigated through our simulations. In support of this notion, the DFT-calculated barrier ($\Delta G^{\ddagger}$) of the energy transfer for **9,10-AQ** to produce $^1O_2$ is unrealistically high at 138.9 kcal/mol if intramolecular

https://doi.org/10.1021/jacsau.2c00281
JACS Au 2022, 2, 2001−2012

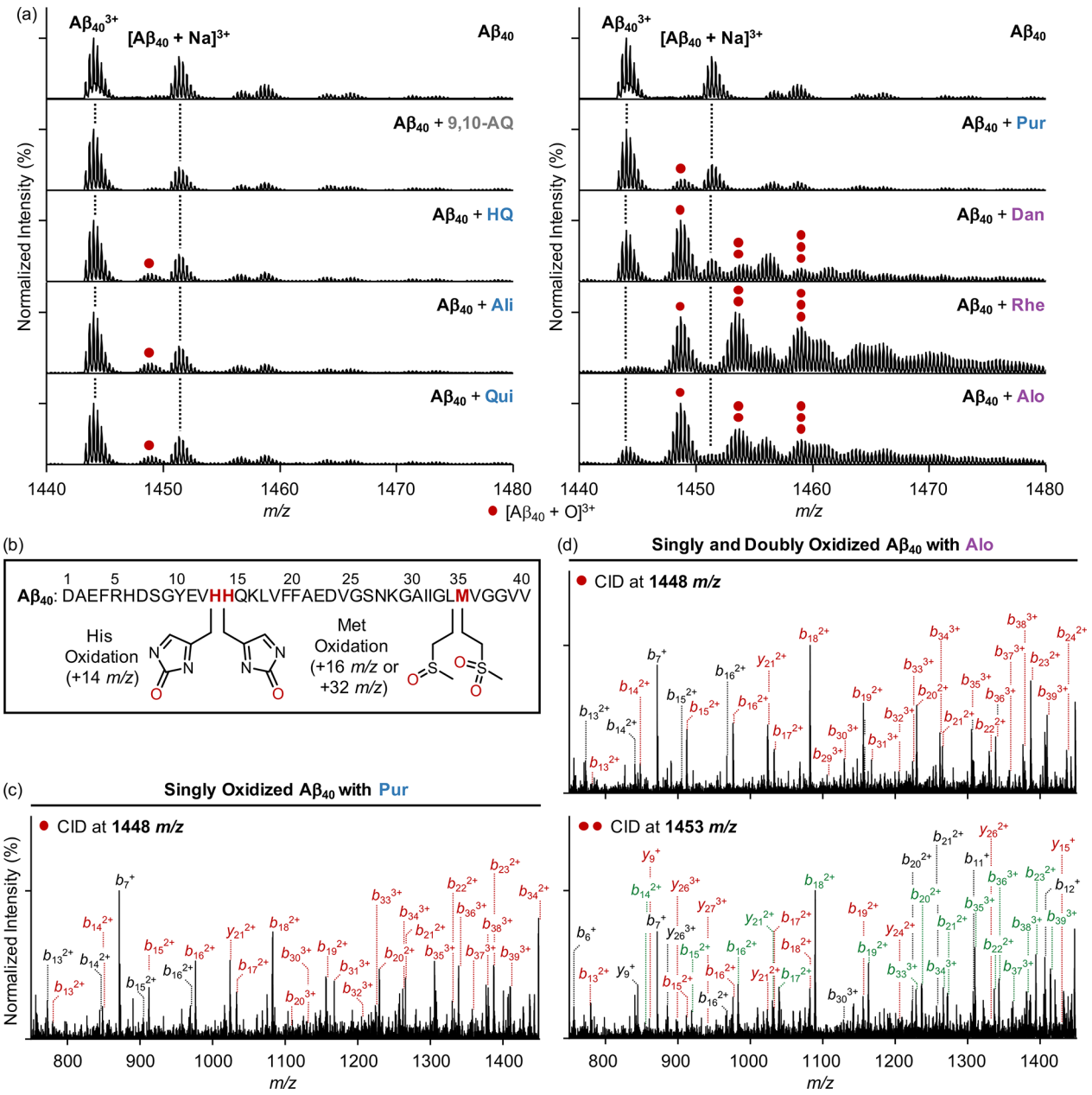

Figure 3. Analysis of Aβ_{40} species produced by treatment of the **AQ** series with light exposure by ESI−MS and ESI−MS^2. (a) ESI−MS spectra of the samples containing Aβ_{40} and compounds with and without light treatment. The number of red dots represents the number of oxygen atoms incorporated into the Aβ_{40} monomer $[A\beta_{40} + nO]^{3+}$ (n = 1, 2, or 3). (b) Sequence of Aβ_{40} and structures of oxidized His and Met residues. (c, d) ESI−MS^2 analyses of the singly oxidized peak (m/z = 1448) obtained by treatment of **Pur** as well as the singly and doubly oxidized peaks (m/z = 1448 and 1453, respectively) generated upon incubation with **Alo**. In the ESI−MS^2 studies, monooxidized and dioxidized b and y ions are illustrated in red and green, respectively. Conditions: [Aβ_{40}] = 25 μM; [compound] = 50 μM; 20 mM ammonium acetate (1% v/v DMSO), pH 7.4; 37 °C; 3 h; constant agitation (250 rpm); Kessil lamp (467 nm) for 1 h. The samples were diluted by 5-fold with H_2O before injection into the mass spectrometer.

hydrogen transfer is not considered. The incorporation of the hydroxyl moiety enables intramolecular hydrogen transfer and reduces the triplet energy transfer barrier considerably, suggesting that hydroxyanthraquinones are suitable scaffolds for $^1O_2$ production. Specifically, calculations on **Group A** (**HQ**, **Ali**, **Qui**, and **Pur**; Figure 1a) that share a common backbone of 1-hydroxyl group next to the ketone functionality reveal low energy transfer barriers ranging from 1.3 up to 11.2 kcal/mol. The molecules in **Group B** (**Dan**, **Rhe**, and **Alo**) with 1- and 8-hydroxyl moieties are predicted to be most efficient and barrierless.

We questioned why the position of hydroxyl groups has such a dramatic impact on the energy transfer barriers toward $^3O_2$ excitation. The triplet energy transfer barrier can be divided into two principal components: thermodynamic driving force (ΔG) and reorganization energy (λ).[67−69] ΔG is the energy difference between the singlet−triplet energy gap of the donor and the acceptor. Comparing the frontier molecular orbitals of the donor scaffolds, all of our selected **AQ** derivatives bear delocalized singly occupied molecular orbital (SOMO) in their triplet state, as presented in Figure S4. The molecules in **Group A** present a smaller singlet−triplet energy gap of the

https://doi.org/10.1021/jacsau.2c00281
JACS Au 2022, 2, 2001−2012

donor where ΔG varies from −13.3 to 3.6 kcal/mol. This small energy gap is due to the biased position of electron-donating groups and the resulting localized highest occupied molecular orbital (HOMO), which leads to a relatively unstable singlet ground state. The consequence is dramatic for the deprotonated **Ali** and **Pur** (ΔG of 3.6 kcal/mol and −0.1 kcal/mol, respectively) possessing phenolate moieties with a strong electron-donating character at neutral pH.[58] In contrast to **Group A**, the compounds in **Group B** retain symmetrically positioned hydroxyl groups with delocalized HOMO in the singlet ground state maintaining the singlet−triplet energy gap to a range of −16.2 to −14.7 kcal/mol. Another factor in determining the barrier is λ associated with structural changes required for the energy transfer. Ranging from 24.6 to 38.5 kcal/mol, the molecules in **Group A** generally require higher λ values than those in **Group B** that show λ values in the range of 16.8 to 17.2 kcal/mol. To better understand this trend, **HQ** (λ = 24.6 kcal/mol) and **Dan** (λ = 16.8 kcal/mol) were chosen to represent molecules in **Group A** and **Group B**, respectively, as depicted in Figure 2c. The hydrogen bond in ^{3}**HQ** shortens from 1.64 to 0.99 Å during donor relaxation, while the hydrogen bond involved in the hydrogen transfer in ^{3}**Dan** displays a smaller change from 1.58 to 0.99 Å, indicating a reduced reorganization penalty compared to that of ^{3}**HQ**. Two explanations can be offered to unveil the role of the additional hydroxyl group at the R_1 position of **Dan**. In the context of intramolecular resonance-assisted hydrogen bonding, the extra hydroxyl functionality can serve as a π-electron-donating group to strengthen the hydrogen bond motif and, subsequently, shorten it.[70] As another aspect, the additional hydrogen bond donor can withdraw the electron density from the interacting hydroxyl group and lower its pK_a facilitating the hydrogen transfer process back to the singlet ground state structure. We reoptimized the triplet structure of ^{3}**Dan** with the supplementary hydroxyl group to face the opposite direction and observed a slight elongation of the hydrogen bond length to 1.61 Å, which validates the dual effect of the hydroxyl group at R_1 in **Group B**, as described in Figure S5.

An alternative mechanism can be proposed for the excitation and relaxation of the photosensitizers during the triplet energy transfer: the stepwise procedure where the vertical relaxation of the triplet state comes first and RIHT comes later, as shown in Figure S6. Note that the mechanism of the concerted or stepwise pathway is still under debate because of the undetectable phosphorescence for hydroxyanthraquinones. Two types of vertical relaxation were examined through DFT and time-dependent density functional theory (TD-DFT) calculations: the **AQ** series that (i) undergoes ESIHT in a stepwise manner or (ii) does not transfer their hydrogen upon excitation. In both of these cases, the reorganization energy is negligible and the singlet−triplet energy gap is the only factor that determines the triplet energy transfer. According to our calculations, the ESIHT-assisted models exhibit an adequate energy gap to facilitate the triplet energy process. **Ali**, **Qui**, and **Pur** have an energy gap ranging from 10.9 to 19.9 kcal/mol that is insufficient for converting $^3O_2$ to $^1O_2$, while the energy gap of **HQ**, **Dan**, **Rhe**, and **Alo** ranges from 21.6 to 23.2 kcal/mol comparable to the energy of 22.5 kcal/mol needed to activate inert $^3O_2$. On the other hand, our hypothetical model that does not go through ESIHT and directly to intersystem crossing yields a larger singlet−triplet energy gap. **HQ** has an energy gap of 42.6 kcal/mol, but **Ali** and **Pur** present an energy gap between 12.5 and 18.9 kcal/mol that is too small. **Dan**, **Rhe**, and **Alo** have energy gaps in the range of 40.6 to 43.4 kcal/mol, rendering them incompetent to achieve effective triplet energy transfer to the oxygen acceptor. Therefore, ESIHT plays a significant role for the **AQ** series not only in the concerted but also in the stepwise mechanism to become appropriate photosensitizers by controlling the singlet−triplet energy gap. Taken together, our computational studies highlight the importance of additional hydroxyl groups and reveal that the position of hydrogen bond donors is key to facilitate the triplet energy transfer.

Aβ Oxidation

To determine whether the **AQ** series can oxidatively modify metal-free Aβ and metal−Aβ with photoirradiation under aerobic conditions, the resultant Aβ species were analyzed by electrospray ionization−mass spectrometry (ESI−MS) and tandem MS (ESI−MS^2). As displayed in Figures 3a and S7, no significant change in metal-free Aβ_{40} was observed in the absence of light. Upon photoactivation of the **AQ** series, the peaks corresponding to oxidized Aβ_{40} species were monitored. The parent molecule **9,10-AQ** did not affect Aβ_{40} despite light exposure. When **HQ**, **Ali**, **Qui**, and **Pur** (**Group A**) were exposed to Aβ_{40}, a new peak was detected at 1,448 m/z, indicative of the incorporation of a single oxygen atom into monomeric Aβ_{40}. In the case of **Dan**, **Rhe**, and **Alo** (**Group B**), three new peaks were detected at 1,448, 1,453, and 1,459 m/z corresponding to the singly, doubly, and triply oxidized Aβ_{40} monomers, respectively. The singly, doubly, or triply oxidized Aβ_{40} monomer induced by the light-activated **AQ** series was also noticed in both Zn(II)−Aβ_{40} and Cu(II)−Aβ_{40}, as shown in Figure S8.

The peaks assigned to oxidized Aβ_{40} species generated by photoactivation were further probed by ESI−MS^2 to identify the oxidized amino acid residues (Figure 3b). Aβ_{40} peptides photooxygenated with **Pur** (**Group A**) and **Alo** (**Group B**) to different extents were selected for tandem MS measurements. Figure 3c exemplifies the collision-induced dissociation (CID) experiments on the singly oxidized peak of Aβ_{40} (1,448 m/z) obtained by photoexcited **Pur**. We observed b fragments from b_{13} in their nonoxidized and oxidized forms, implying that **Pur** oxidizes either His13, His14, or Met35. It should be noted that the oxidation is unable to simultaneously modify more than one residue. On the contrary, as disclosed in Figure 3d, ESI−MS^2 studies on the singly and doubly oxidized peaks verified that **Alo** can concurrently oxidize all three aforementioned amino acid residues. The fragmentation analysis on the singly oxidized Aβ_{40} by **Alo** was identical to the results obtained by **Pur**. For the doubly oxidized Aβ_{40}, we could not monitor oxidized fragments smaller than b_{13}, and doubly oxidized forms were detected from b ions larger than b_{13}. Note that the Met residue was oxidized to sulfone in the doubly oxidized Aβ_{40}. Overall, our MS studies substantiate that the **AQ** series can possibly oxidize Aβ at the His13, His14, and Met35 residues to varying degrees.

Influence on Aβ Aggregation

To test if the different degree of Aβ oxidation by light activation of the molecules in **Group A** and **Group B** alters the aggregation of both metal-free Aβ and metal−Aβ in a detectable manner, the molecular weight (MW) distribution of the resultant Aβ species was first analyzed by gel electrophoresis with Western blotting (gel/Western blot) using an anti-Aβ antibody (6E10). The morphological change of metal-free Aβ or metal−Aβ aggregates produced by

https://doi.org/10.1021/jacsau.2c00281
JACS Au 2022, 2, 2001−2012

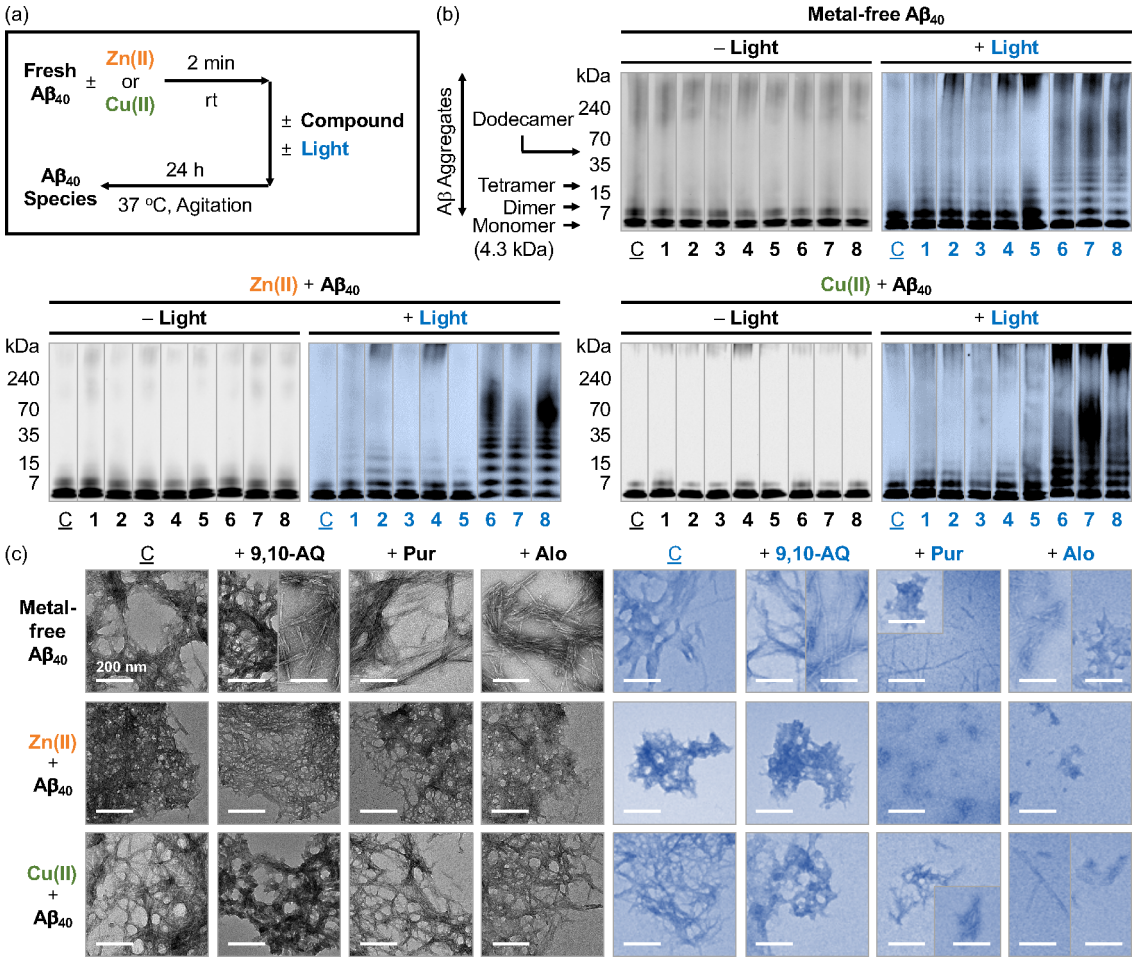

Figure 4. Impact of the **AQ** series on the formation of metal-free or metal-treated Aβ_{40} aggregates with and without light activation. (a) Scheme of the inhibition experiments. (b) Gel/Western blots (anti-Aβ antibody, 6E10) of the resultant Aβ_{40} species upon incubation of metal-free and metal-added Aβ_{40} with and without treatment of compounds and light. Lanes: (C) Aβ_{40}; (**1**) Aβ_{40} + **9,10-AQ**; (**2**) Aβ_{40} + **HQ**; (**3**) Aβ_{40} + **Ali**; (**4**) Aβ_{40} + **Qui**; (**5**) Aβ_{40} + **Pur**; (**6**) Aβ_{40} + **Dan**; (**7**) Aβ_{40} + **Rhe**; (**8**) Aβ_{40} + **Alo**. (c) TEM images of the aggregates produced upon 24 h incubation of metal-free and metal-treated Aβ_{40} with and without the **AQ** series in the absence and presence of light. Conditions: [Aβ_{40}] = 25 μM; [M(II)] = 25 μM; [compound] = 50 μM; 20 mM HEPES (1% v/v DMSO), pH 7.4 [for metal-free or Zn(II)-containing samples] or pH 6.6 [for Cu(II)-added samples], 150 mM NaCl; 37 °C; 24 h; constant agitation (250 rpm); Kessil lamp (467 nm) for 1 h. Scale bar = 200 nm.

treatment of the **AQ** series was visualized with transmission electron microscopy (TEM). Aβ aggregates larger than ca. 270 kDa are not detectable in gel/Western blot but can be probed by TEM. In this work, we conducted two experiments: (i) inhibition experiments for determining the influence of the **AQ** series on the formation of Aβ aggregates; (ii) disaggregation experiments for assessing the ability of the **AQ** series to disassemble preformed Aβ aggregates.

In the inhibition experiments, metal-free Aβ or metal−Aβ was freshly prepared and treated for 24 h with the **AQ** series, as shown in Figure 4a. For light-exposed samples, Aβ species added with the **AQ** series were photoirradiated for 1 h prior to 24 h incubation. As portrayed in Figure 4b, under dark conditions (gray gels), no significant change in the MW distribution of both metal-free Aβ_{40} and metal−Aβ_{40} was observed even with the addition of the **AQ** series. Notably, in the presence of light, the resultant Aβ_{40} species with the **AQ** series (blue gels) showed a divergent MW distribution, relative to Aβ_{40} only. Treatment of metal-free Aβ_{40} with light-activated **9,10-AQ**, **HQ**, **Ali**, **Qui**, and **Pur** gave rise to increased signal intensities between ca. 15−35 kDa. Note that the **AQ** series can produce superoxide anion radicals;[71] however, we could not monitor them because the excitation and emission wavelengths used for the assays overlapped with those of the compounds. On the contrary, the illuminated Aβ_{40} samples with **Dan**, **Rhe**, and **Alo** greatly affected the MW distribution exhibiting new gel bands throughout ca. 15−240 kDa. Smearing bands over ca. 240 kDa were spotted for the samples added with both **Group A** and **Group B** indicating that the light-driven oxidation of metal-free Aβ_{40} leads to smaller peptide ensembles that can penetrate the gel matrix. In the inhibition experiments with Zn(II)−Aβ_{40}, **9,10-AQ**, **HQ**, **Ali**, **Qui**, and **Pur** upon photoactivation mildly affected the MW distribution while **Dan**, **Rhe**, and **Alo** significantly enhanced the intensities of the bands between ca. 15−240 kDa. Various aggregates were detected upon incubation of Cu(II)−Aβ_{40} with photoreactive **Dan**, **Rhe**, and **Alo**, but moderate effects were identified with the illumination of the rest of the **AQ** series.

As described in Figure 4c, metal-free Aβ_{40} and metal−Aβ_{40} aggregates generated with and without the treatment of **9,10-AQ**, **Pur**, or **Alo** were further examined by TEM. **9,10-AQ**, **Pur**, and **Alo** were chosen as the representative molecules of **Parent**, **Group A**, and **Group B**, respectively. Without light,

https://doi.org/10.1021/jacsau.2c00281
JACS Au 2022, 2, 2001−2012

thick fibrils were formed by incubation of metal-free Aβ_{40} in the presence of all three compounds, compared to fibrillary aggregates produced in the sample of metal-free Aβ_{40} only. Morphologies of the resultant metal−Aβ_{40} aggregates were not significantly changed even with the compounds, however. This suggests that the **AQ** backbone itself may interact with metal-free Aβ_{40} and affect its aggregation. When **9,10-AQ** was incubated with metal-free Aβ_{40} with photoirradiation, long and thick fibrils as well as similar fibrils to those formed from Aβ_{40} only were detected. The conformational transformation of metal-free Aβ_{40} by photoexcited **Pur** and **Alo** was more noticeable than that by **9,10-AQ**, resulting in smaller and thinner aggregates. In the case of metal−Aβ_{40} species, small amorphous assemblies and thin fibrils were visualized with the illumination of **Pur** and **Alo**, but **9,10-AQ** did not noticeably alter their morphologies. These amorphous aggregates are reported to be less toxic than structured assemblies.[13,15,17] Modest or no changes found in the structures of metal-free and metal-bound Aβ_{40} species with photoactivated **9,10-AQ** denote the importance of efficient $^1O_2$ production in modifying their aggregation pathways.

Inhibition experiments were also conducted employing Aβ_{42} (Figure S9a). As described in Figure S9b, the application of light with **9,10-AQ** toward metal-free Aβ_{42} enhanced the band intensity in the high MWs (ca. over 70 kDa). **HQ** and **Ali** did not significantly change MW distribution with photoirradiation. The addition of light-exposed **Qui**, **Pur**, and **Dan** reduced the intensities of the bands in the lower MW region (ca. below 15 kDa) but increased them in the higher MW region (ca. over 70 kDa). This phenomenon was distinct from the samples of **Rhe** and **Alo** with light. In the presence of Zn(II), smearing bands emerged in the case of **Pur**, **Dan**, **Rhe**, and **Alo** throughout ca. 4−270 kDa. In **Ali**- and **Qui**-added samples, a new band at ca. 7 kDa and amplified the intensities of bands over ca. 35 kDa were monitored. Such change of the band above ca. 70 kDa was also observed upon treatment of **9,10-AQ** and **HQ**. The Cu(II)-added samples with the photoilluminated **AQ** series presented the changes in the MW distribution to different extents. Figure S9c illustrates the TEM results of the inhibition experiments using Aβ_{42}. Similar to Aβ_{40}, TEM studies showed that **9,10-AQ**, **Pur**, and **Alo** did not noticeably alter the morphologies of metal-free Aβ_{42} and metal−Aβ_{42} aggregates without light. The size of metal-free Aβ_{42} and metal−Aβ_{42} aggregates was greatly diminished by photoexcited **Alo**, and thinner fibrils and smaller aggregates were spotted by the addition of **Pur**, compared to compound-free and metal-treated Aβ_{42} aggregates.

Moving forward, as depicted in Figures S10 and S11, metal-free Aβ or metal−Aβ was preincubated for 24 h to form peptide aggregates and the **AQ** series was treated with and without 1 h photoexcitation followed by incubation for an additional 24 h. The gel/Western blots in the disaggregation experiments afforded shifts in the MW distribution of Aβ species to various degrees upon photosensitization of the **AQ** series. Specifically, the MW distribution of preformed metal-free Aβ_{40} aggregates was influenced by **9,10-AQ**, **HQ**, **Ali**, **Qui**, **Pur**, **Dan**, and **Rhe** exhibiting new bands between ca. 15−35 kDa. Light-exposed **Ali**, **Qui**, **Pur**, **Dan**, **Rhe**, and **Alo** showed dimmer or no bands in the MW region below ca. 7 kDa. Substantial MW changes of Zn(II)−Aβ_{40} aggregates incubated with **Dan**, **Rhe**, and **Alo** were observed with new bands throughout ca. 15−270 kDa. In the case of **Qui** and **Pur**, the intensities at ca. 7 kDa and above 240 kDa were increased, but photoactivated **9,10-AQ**, **HQ**, and **Ali** manifested a less pronounced impact on the MW distribution. The gel/Western blot of preformed Cu(II)−Aβ_{40} aggregates also indicated an amplified variation in the MW distribution with **Dan**, **Rhe**, and **Alo**, while the treatment of **9,10-AQ** and the molecules in **Group A** resulted in minor or no changes. For metal-free Aβ_{42} aggregates, we were not able to detect a significant MW change with **9,10-AQ**, but slight alterations were found with **HQ** and **Ali**. The addition of **Qui** and **Pur** displayed lower band intensities below ca. 15 kDa. On the other hand, the intensities of the bands throughout the detectable region observed in the sample of Aβ_{42} only were all diminished in the presence of **Dan**, **Rhe**, and **Alo**. Likewise, the MW distribution of metal−Aβ_{42} aggregates with photoactivated **9,10-AQ** was negligibly varied. Against Zn(II)−Aβ_{42} aggregates, the illumination of **Group A** and **Group B** increased the intensity in the higher-order region above ca. 35 kDa. Furthermore, **HQ** and **Qui** produced a new band at ca. 7 kDa with smearing near ca. 15 kDa. **Pur**, **Dan**, **Rhe**, and **Alo** decreased the intensity below ca. 15 kDa. A change in the MW distribution of Cu(II)−Aβ_{42} aggregates was also monitored by treatment of **Group A** and **Group B** in different ranges. Photoactivated **HQ** lowered the intensity between ca. 7−35 kDa, where the bands in the corresponding region became more obscure for **Ali**, **Qui**, and **Pur**. **Dan** resulted in the smearing throughout ca. 7−240 kDa while the bands almost disappeared in the region below ca. 70 kDa for Cu(II)−Aβ_{42} aggregates added with **Rhe** and **Alo**. As presented in Figures S10c and S11c, the fibrillary aggregates of metal-free and metal-bound Aβ_{40} and Aβ_{42} were monitored by treatment of compounds without light, similar to those of compound-free samples. In contrast, thin and short fibrils were detected when **Pur** was incubated and photoexcited with preformed metal-free and metal-bound Aβ aggregates, presenting their morphological changes, different from **9,10-AQ** that showed fibrillary aggregates. When **Alo** was added with preformed metal-free Aβ and Cu(II)−Aβ aggregates upon light activation, thick and well-ordered fibrils without and with amorphous aggregates, respectively, were visualized, and small-sized Aβ aggregates were indicated in the presence of Zn(II).

Taken together, the gel/Western blot and TEM studies implicitly demonstrate the ability of photoexcited **AQ** series for modulating the formation of metal-free Aβ or metal−Aβ aggregates as well as the disassembly of preformed metal-free or metal-added Aβ aggregates. The impact of photoreactive **AQ** series against diverse Aβ species reflects the significance of $^1O_2$ production and the number of oxygen atoms incorporated into Aβ; thus, the compounds in **Group B** are able to remarkably modify the aggregation pathways of both metal-free Aβ and metal−Aβ. Furthermore, taking account to minimum changes noticed in the parent structure **9,10-AQ**, these in vitro aggregation investigations reveal the relationship between the structural features (e.g., the position and number of hydroxyl groups placed in the framework) of the **AQ** series and the modulatory reactivity toward the aggregation of metal-free Aβ and metal−Aβ. Note that such structural variations can change photophysical properties of compounds, with their direct contacts on Aβ species (vide infra).

Biological Efficacies

The cell viability and BBB permeability of the **AQ** series were examined prior to in vivo studies. Photodegradation of photosensitizers during illumination was reported to yield unidentified fragments that can cause toxicity.[72] Thus, the

https://doi.org/10.1021/jacsau.2c00281
JACS Au 2022, 2, 2001−2012

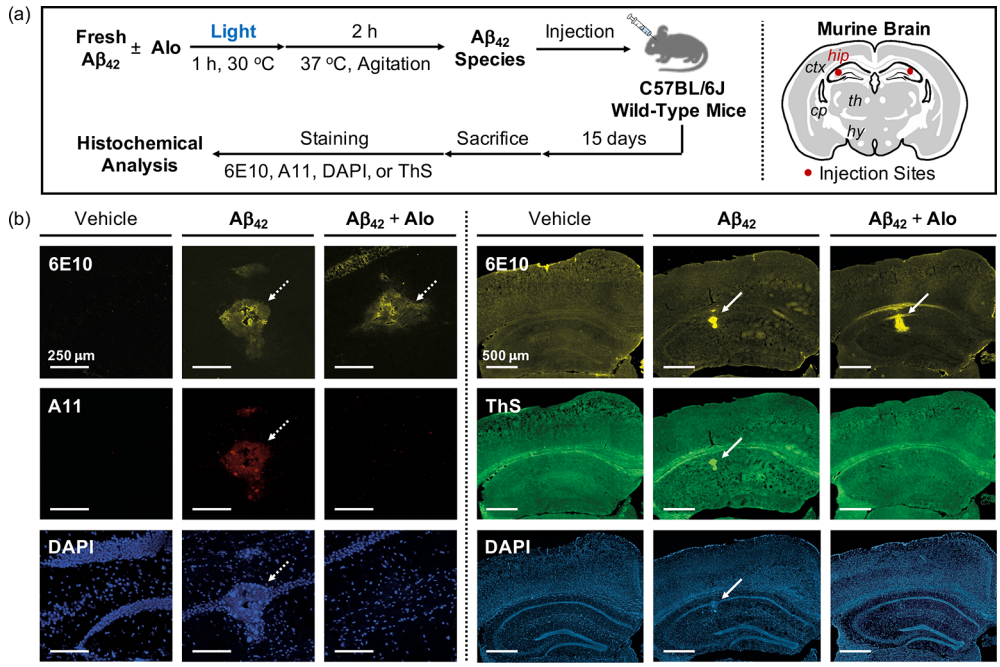

Figure 5. Detection of the Aβ_{42} aggregate deposition in murine brains injected with photoactivated **Alo**-treated Aβ_{42} species. (a) Schematic description of histochemical studies and injection sites in the brain. Hippocampus (*hip*), cortex (*ctx*), thalamus (*th*), caudate putamen (*cp*), and hypothalamus (*hy*) are shown. (b) Microscopic images of the hippocampi of C57BL/6J mice injected with vehicle, Aβ_{42}, or **Alo**-treated Aβ_{42}. Aβ species were prepared in 20 mM HEPES, pH 7.4, 150 mM NaCl (1% v/v DMSO; vehicle) and visualized by immunostaining [primary antibodies, 6E10 (anti-Aβ antibody; yellow) and A11 (antioligomer antibody; red) with fluorescent-conjugated secondary antibodies] or fluorescent dyes [ThS for Aβ fibrils (green) and DAPI for fibrillary Aβ and nucleus (blue)]. Images were taken by a confocal microscope (left; ×10) or a scanning microscope (right; ×10). Detected amyloid species are marked with white arrows. Scale bars = 250 and 500 μm for confocal or scanning microscopies, respectively. Animal number: n = 4 (for Aβ_{42} and **Alo**-added Aβ_{42}) and n = 3 (for vehicle).

toxicity of the compounds prepared with and without photoirradiation was determined in human neuroblastoma SH-SY5Y cells by the MTT assay [MTT = 3-(4,5-dimethylthiazol-2-yl)-2,5-diphenyltetrazolium bromide]. As described in Figure S12, the cells in the presence of both **Group A** and **Group B** without photoactivation exhibited greater survival of over ca. 80% at up to 25 μM. The parent moiety **9,10-AQ** displayed over 70% cell viability. Intriguingly, the toxicity of all molecules preilluminated for 1 h before 24 h incubation was lowered by up to ca. 14% at 25 μM. This suggests that the **AQ** series does not yield more toxic products upon photoactivation.

Crossing the BBB is an essential factor for chemical reagents to be utilized in the brain.[73] Thus, the brain uptake of the **AQ** series was predicted by the parallel artificial membrane permeability assay adapted for the BBB.[74,75] As summarized in Table S1, most of the molecules selected in this study were expected to have sufficient BBB penetration with a $-\log P_e$ value below 5.4 except for **9,10-AQ** [5.54 (±0.11)] and (**Rhe** [5.97 (±0.03)]. The permeability of **9,10-AQ** could not be determined due to limited solubility in water. Moving forward, we chose to examine **Alo** in histochemical investigations in vivo because it showed a relatively high $^1O_2$ quantum yield in the **AQ** series, significant modulatory impact on Aβ aggregation, relatively low cytotoxicity, and potential BBB permeability.

To assess the aggregation propensity of both Aβ_{40} and Aβ_{42} species treated with **Alo** and light in the brain, we conducted histochemical studies on the brain samples injected with **Alo**-treated Aβ species. As illustrated in Figures S13a and 5a, Aβ_{40} and Aβ_{42} were freshly prepared in 20 mM HEPES, pH 7.4, 150 mM NaCl (1% v/v DMSO; vehicle), exposed to light for 1 h with and without **Alo**, incubated for an additional 2 h, and directly injected into the hippocampus of murine brains. The hippocampal region is vital for memory formation and retrieval in both murine and human brains and is highly affected by Aβ aggregates formed during the progression of AD.[76−78] 15 days after the injection, the brain sections were stained with antibodies or fluorescence dyes to determine the deposition of Aβ aggregates in the hippocampus. As displayed in Figures S13b and 5b, both compound-free and **Alo**-added Aβ species were safely injected into the hippocampal region, as confirmed by immunostaining with an anti-Aβ primary antibody (6E10).[79,80] As expected, the brain samples administered with compound-free Aβ species exhibited Aβ aggregates such as oligomers or fibrils visualized with an antibody and fluorescent dyes [e.g., detection of Aβ oligomers with an antioligomer antibody (A11)[81] and Aβ fibrils with thioflavin-S (ThS)[82,83] or DAPI[84,85]]. Note that DAPI is also capable of immunostaining cellular nuclei.[84,85] Interestingly, oligomeric and fibrillar aggregates were not significantly visible in the brain samples injected with Aβ species oxidized by photoactivated **Alo**. Given that Aβ oligomers are reported to be neurotoxic by various pathways (e.g., interacting with cellular membranes and damaging intracellular organelles)[7,86,87] and the accumulation of fibrillary amyloid plaques is another pathogenic feature upon the progression of AD,[88,89] these overall results imply that the off-pathway assembly of the resultant oxidized Aβ species by **Alo** with photoactivation takes place in vivo.

https://doi.org/10.1021/jacsau.2c00281
JACS Au 2022, 2, 2001−2012

CONCLUSIONS

Regulating the aggregation of Aβ peptides with synthetic small chemical tools has been the long-lasting interest and challenge to alleviate the progression of AD.[7] Incorporation of oxygen atoms in early stage amyloid species as well as mature fibrils resulted in dramatic changes of their morphologies and toxicity while preventing the restoration of their original form. There has been controversy of the specific role of Aβ in AD, but recent reports continue to emphasize the necessity of our study.[90] The demand of finding appropriate reagents oxidatively modifying pathological factors in AD requires both effective $^1O_2$ production and nontoxic byproducts. Our structure-based computational modeling of small **AQ**-based molecules highlights the importance of the adequate level of the singlet−triplet energy gap associated with the reorganization energy throughout the ESIHT process. These conditions were met by incorporating additional hydroxyl groups to form two quasi-ring moieties that facilitate $^1O_2$ production. Spectroscopic and biochemical studies demonstrate the enhanced photoreactivity of **AQ**-based reagents with two quasi-rings mediated by hydrogen bonding against metal-free Aβ and metal−Aβ, compared to the molecules that possess one or no intramolecular quasi-ring. The **AQ** series also displayed relatively lower cellular toxicity upon photoactivation. In the brains of mice, Aβ species generated by **Alo** with light exposure exhibited minimum aggregation into amyloid assemblies such as oligomers or fibrils known to be linked to the pathology of AD.

Furthermore, selectivity is another crucial aspect for Aβ-targeting small molecules. As illustrated in Figure S14, **Pur** and **Alo** could bind with Aβ_{40} species, as observed by docking studies, where both hydroxyl groups and the three-membered ring can interact with hydrophilic and hydrophobic residues in Aβ, respectively. This interplay may indicate the importance of both hydrophilic and hydrophobic structural moieties of the **AQ** series for targeting the self-recognition site (i.e., LVFFA; Figure 1b) of Aβ and affecting its aggregation pathways. Like Aβ oxidation, **Alo** has the ability to oxidize other disease-related amyloidogenic proteins or peptides such as α-synuclein and human islet amyloid polypeptide (hIAPP) and modify their aggregation pathways, as depicted in Figure S15. The oxidation of each peptide in a mixture of Aβ_{40} and hIAPP was further monitored. Thus, our **AQ** series should be optimized to achieve the selectivity against Aβ species for biological applications. Overall, our combined experimental and computational studies illuminate how compact photoactivable molecules that can readily modify amyloidogenic peptides and, consequently, control their aggregation process can be rationally developed.

ASSOCIATED CONTENT

Supporting Information

The Supporting Information is available free of charge at https://pubs.acs.org/doi/10.1021/jacsau.2c00281.

Experimental Section, Table S1, and Figures S1−S15 (PDF)

AUTHOR INFORMATION

Corresponding Authors

Seung-Hee Lee − *Department of Biological Sciences, Korea Advanced Institute of Science and Technology (KAIST), Daejeon 34141, Republic of Korea*; Email: shlee1@kaist.ac.kr

Mu-Hyun Baik − *Department of Chemistry, Korea Advanced Institute of Science and Technology (KAIST), Daejeon 34141, Republic of Korea; Center for Catalytic Hydrocarbon Functionalizations, Institute for Basic Science (IBS), Daejeon 34141, Republic of Korea;* orcid.org/0000-0002-8832-8187; Email: mbaik2805@kaist.ac.kr

Mi Hee Lim − *Department of Chemistry, Korea Advanced Institute of Science and Technology (KAIST), Daejeon 34141, Republic of Korea;* orcid.org/0000-0003-3377-4996; Email: miheelim@kaist.ac.kr

Authors

Mannkyu Hong − *Department of Chemistry, Korea Advanced Institute of Science and Technology (KAIST), Daejeon 34141, Republic of Korea; Center for Catalytic Hydrocarbon Functionalizations, Institute for Basic Science (IBS), Daejeon 34141, Republic of Korea;* orcid.org/0000-0002-7770-1230

Mingeun Kim − *Department of Chemistry, Korea Advanced Institute of Science and Technology (KAIST), Daejeon 34141, Republic of Korea*

Jiwon Yoon − *Department of Biological Sciences, Korea Advanced Institute of Science and Technology (KAIST), Daejeon 34141, Republic of Korea*

Complete contact information is available at: https://pubs.acs.org/10.1021/jacsau.2c00281

Author Contributions

‖M.H. and M.K. contributed equally to this work.

Notes

The authors declare no competing financial interest.

ACKNOWLEDGMENTS

This work was supported by the National Research Foundation of Korea (NRF) grant funded by the Korean government [NRF-2022R1A3B1077319 and NRF-2016R1A5A1009405 (M.H.L.); NRF-2021R1A2C3012159 (S.-H.L.)] and the Institute for Basic Science (IBS-R010-A1) in Korea (to M.-H.B.). We thank Professor Youngmin You (Ewha Womans University) and Dr. Jiyong Park (IBS) for fruitful discussions on photophysical properties and computational analysis, respectively.

REFERENCES

(1) Hoyt, E. A.; Cal, P. M. S. D.; Oliveira, B. L.; Bernardes, G. J. L. Contemporary approaches to site-selective protein modification. *Nat. Rev. Chem.* **2019**, *3*, 147−171.

(2) Krall, N.; da Cruz, F. P.; Boutureira, O.; Bernardes, G. J. L. Site-selective protein-modification chemistry for basic biology and drug development. *Nat. Chem.* **2016**, *8*, 103−113.

(3) Conibear, A. C. Deciphering protein post-translational modifications using chemical biology tools. *Nat. Rev. Chem.* **2020**, *4*, 674−695.

(4) Milczek, E. M. Commercial applications for enzyme-mediated protein conjugation: new developments in enzymatic processes to deliver functionalized proteins on the commercial scale. *Chem. Rev.* **2018**, *118*, 119−141.

(5) Walsh, C. T. *Posttranslational modification of proteins: expanding natures inventory*; Roberts and Company Publishers, 2006; pp 1−462.

(6) Boutureira, O.; Bernardes, G. J. L. Advances in chemical protein modification. *Chem. Rev.* **2015**, *115*, 2174−2195.

(7) Savelieff, M. G.; Nam, G.; Kang, J.; Lee, H. J.; Lee, M.; Lim, M. H. Development of multifunctional molecules as potential therapeutic candidates for Alzheimer's disease, Parkinson's disease, and amyotrophic lateral sclerosis in the last decade. *Chem. Rev.* **2019**, *119*, 1221−1322.
(8) Suh, J.-M.; Kim, G.; Kang, J.; Lim, M. H. Strategies employing transition metal complexes to modulate amyloid-β aggregation. *Inorg. Chem.* **2019**, *58*, 8−17.
(9) Heo, Y.; Kim, K.; Kim, J.; Jang, J.; Park, C. B. Near-infrared-active copper bismuth oxide electrodes for targeted dissociation of Alzheimer's β-amyloid aggregates. *ACS Appl. Mater. Interfaces* **2020**, *12*, 23667−23676.
(10) Han, J.; Lee, H. J.; Kim, K. Y.; Nam, G.; Chae, J.; Lim, M. H. Mechanistic approaches for chemically modifying the coordination sphere of copper−amyloid-β complexes. *Proc. Natl. Acad. Sci. U. S. A.* **2020**, *117*, 5160−5167.
(11) Derrick, J. S.; Lee, J.; Lee, S. J. C.; Kim, Y.; Nam, E.; Tak, H.; Kang, J.; Lee, M.; Kim, S. H.; Park, K.; Cho, J.; Lim, M. H. Mechanistic insights into tunable metal-mediated hydrolysis of amyloid-β peptides. *J. Am. Chem. Soc.* **2017**, *139*, 2234−2244.
(12) Li, C.; Wang, J.; Liu, L. Alzheimer's therapeutic strategy: photoactive platforms for suppressing the aggregation of amyloid β protein. *Front. Chem.* **2020**, *8*, 509.
(13) Kim, M.; Kang, J.; Lee, M.; Han, J.; Nam, G.; Tak, E.; Kim, M. S.; Lee, H. J.; Nam, E.; Park, J.; Oh, S. J.; Lee, J.-Y.; Lee, J.-Y.; Baik, M.-H.; Lim, M. H. Minimalistic principles for designing small molecules with multiple reactivities against pathological factors in dementia. *J. Am. Chem. Soc.* **2020**, *142*, 8183−8193.
(14) Nam, E.; Derrick, J. S.; Lee, S.; Kang, J.; Han, J.; Lee, S. J. C.; Chung, S. W.; Lim, M. H. Regulatory activities of dopamine and its derivatives toward metal-free and metal-induced amyloid-β aggregation, oxidative stress, and inflammation in Alzheimer's disease. *ACS Chem. Neurosci.* **2018**, *9*, 2655−2666.
(15) Beck, M. W.; Derrick, J. S.; Kerr, R. A.; Oh, S. B.; Cho, W. J.; Lee, S. J. C.; Ji, Y.; Han, J.; Tehrani, Z. A.; Suh, N.; Kim, S.; Larsen, S. D.; Kim, K. S.; Lee, J.-Y.; Ruotolo, B. T.; Lim, M. H. Structure-mechanism-based engineering of chemical regulators targeting distinct pathological factors in Alzheimer's disease. *Nat. Commun.* **2016**, *7*, 13115.
(16) Beck, M. W.; Derrick, J. S.; Suh, J.-M.; Kim, M.; Korshavn, K. J.; Kerr, R. A.; Cho, W. J.; Larsen, S. D.; Ruotolo, B. T.; Ramamoorthy, A.; Lim, M. H. Minor structural variations of small molecules tune regulatory activities toward pathological factors in Alzheimer's disease. *ChemMedChem.* **2017**, *12*, 1828−1838.
(17) Derrick, J. S.; Kerr, R. A.; Nam, Y.; Oh, S. B.; Lee, H. J.; Earnest, K. G.; Suh, N.; Peck, K. L.; Ozbil, M.; Korshavn, K. J.; Ramamoorthy, A.; Prabhakar, R.; Merino, E. J.; Shearer, J.; Lee, J.-Y.; Ruotolo, B. T.; Lim, M. H. A redox-active, compact molecule for cross-linking amyloidogenic peptides into nontoxic, off-pathway aggregates: in vitro and in vivo efficacy and molecular mechanisms. *J. Am. Chem. Soc.* **2015**, *137*, 14785−14797.
(18) Han, J.; Lee, H. J.; Kim, K. Y.; Lee, S. J. C.; Suh, J.-M.; Cho, J.; Chae, J.; Lim, M. H. Tuning structures and properties for developing novel chemical tools toward distinct pathogenic elements in Alzheimer's disease. *ACS Chem. Neurosci.* **2018**, *9*, 800−808.
(19) Ishida, Y.; Tanimoto, S.; Takahashi, D.; Toshima, K. Photo-degradation of amyloid β by a designed fullerene−sugar hybrid. *Med. Chem. Commun.* **2010**, *1*, 212−215.
(20) Lee, B. I.; Lee, S.; Suh, Y. S.; Lee, J. S.; Kim, A.-k.; Kwon, O-Y.; Yu, K.; Park, C. B. Photoexcited porphyrins as a strong suppressor of β-amyloid aggregation and synaptic toxicity. *Angew. Chem., Int. Ed.* **2015**, *127*, 11634−11638.
(21) Kang, J.; Lee, S. J. C.; Nam, J. S.; Lee, H. J.; Kang, M.-G.; Korshavn, K. J.; Kim, H.-T.; Cho, J.; Ramamoorthy, A.; Rhee, H.-W.; Kwon, T.-H.; Lim, M. H. An iridium(III) complex as a photo-activatable tool for oxidation of amyloidogenic peptides with subsequent modulation of peptide aggregation. *Chem. Eur. J.* **2017**, *23*, 1645−1653.
(22) Leung, C.-H.; Zhong, H.-J.; Chan, D. S.-H.; Ma, D.-L. Bioactive iridium and rhodium complexes as therapeutic agents. *Coord. Chem. Rev.* **2013**, *257*, 1764−1776.
(23) Man, B. Y.-W.; Chan, H.-M.; Leung, C.-H.; Chan, D. S.-H.; Bai, L.-P.; Jiang, Z.-H.; Li, H.-W.; Ma, D.-L. Group 9 metal-based inhibitors of β-amyloid (1−40) fibrillation as potential therapeutic agents for Alzheimer's disease. *Chem. Sci.* **2011**, *2*, 917−921.
(24) Wong, C.-Y.; Chung, L.-H.; Lu, L.; Wang, M.; He, B.; Liu, L.-J.; Leung, C.-H.; Ma, D.-L. Dual inhibition and monitoring of β-amyloid fibrillation by a luminescent iridium(III) complex. *Curr. Alzheimer Res.* **2015**, *12*, 439−444.
(25) Gomes, L. M. F.; Bataglioli, J. C.; Storr, T. Metal complexes that bind to the amyloid-β peptide of relevance to Alzheimer's disease. *Coord. Chem. Rev.* **2020**, *412*, 213255.
(26) Bataglioli, J. C.; Gomes, L. M. F.; Maunoir, C.; Smith, J. R.; Cole, H. D.; McCain, J.; Sainuddin, T.; Cameron, C. G.; McFarland, S. A.; Storr, T. Modification of amyloid-beta peptide aggregation via photoactivation of strained Ru(II) polypyridyl complexes. *Chem. Sci.* **2021**, *12*, 7510−7520.
(27) Chung, Y. J.; Lee, C. H.; Lim, J.; Jang, J.; Kang, H.; Park, C. B. Photomodulating carbon dots for spatiotemporal suppression of Alzheimer's beta-amyloid aggregation. *ACS Nano* **2020**, *14*, 16973−16983.
(28) Kim, K.; Lee, S. H.; Choi, D. S.; Park, C. B. Photoactive bismuth vanadate structure for light-triggered dissociation of Alzheimer's β-amyloid aggregates. *Adv. Funct. Mater.* **2018**, *28*, 1802813.
(29) Lee, J. S.; Lee, B. I.; Park, C. B. Photo-induced inhibition of Alzheimer's β-amyloid aggregation in vitro by rose bengal. *Biomaterials* **2015**, *38*, 43−49.
(30) Taniguchi, A.; Sasaki, D.; Shiohara, A.; Iwatsubo, T.; Tomita, T.; Sohma, Y.; Kanai, M. Attenuation of the aggregation and neurotoxicity of amyloid-β peptides by catalytic photooxygenation. *Angew. Chem. Int. Ed.* **2014**, *53*, 1382−1385.
(31) Ni, J.; Taniguchi, A.; Ozawa, S.; Hori, Y.; Kuninobu, Y.; Saito, T.; Saido, T. C.; Tomita, T.; Sohma, Y.; Kanai, M. Near-infrared photoactivatable oxygenation catalysts of amyloid peptide. *Chem.* **2018**, *4*, 807−820.
(32) Lee, B. I.; Suh, Y. S.; Chung, Y. J.; Yu, K.; Park, C. B. Shedding light on Alzheimer's β-amyloidosis: photosensitized methylene blue inhibits self-assembly of β-amyloid peptides and disintegrates their aggregates. *Sci. Rep.* **2017**, *7*, 7523.
(33) Taniguchi, A.; Shimizu, Y.; Oisaki, K.; Sohma, Y.; Kanai, M. Switchable photooxygenation catalysts that sense higher-order amyloid structures. *Nat. Chem.* **2016**, *8*, 974−982.
(34) Bondia, P.; Torra, J.; Tone, C. M.; Sawazaki, T.; del Valle, A.; Sot, B.; Nonell, S.; Kanai, M.; Sohma, Y.; Flors, C. Nanoscale view of amyloid photodynamic damage. *J. Am. Chem. Soc.* **2020**, *142*, 922−930.
(35) Pardridge, W. M. Drug transport across the blood−brain barrier. *J. Cereb. Blood Flow Metab.* **2012**, *32*, 1959−1972.
(36) Zheng, W.; Aschner, M.; Ghersi-Egea, J.-F. Brain barrier systems: a new frontier in metal neurotoxicological research. *Toxicol. Appl. Pharmacol.* **2003**, *192*, 1−11.
(37) Egorova, K. S.; Ananikov, V. P. Toxicity of metal compounds: knowledge and myths. *Organometallics* **2017**, *36*, 4071−4090.
(38) Win-Shwe, T.-T.; Fujimaki, H. Nanoparticles and neurotoxicity. *Int. J. Mol. Sci.* **2011**, *12*, 6267−6280.
(39) Vutskits, L.; Briner, A.; Klauser, P.; Gascon, E.; Dayer, A. G.; Kiss, J. Z.; Muller, D.; Licker, M. J.; Morel, D. R. Adverse effects of methylene blue on the central nervous system. *Anesthesiology* **2008**, *108*, 684−692.
(40) Savelieff, M. G.; Lee, S.; Liu, Y.; Lim, M. H. Untangling amyloid-β, tau, and metals in Alzheimer's disease. *ACS Chem. Biol.* **2013**, *8*, 856−865.
(41) Kepp, K. P. Bioinorganic chemistry of Alzheimer's disease. *Chem. Rev.* **2012**, *112*, 5193−5239.
(42) Bush, A. I.; Tanzi, R. E. Therapeutics for Alzheimer's disease based on the metal hypothesis. *Neurotherapeutics* **2008**, *5*, 421−432.

https://doi.org/10.1021/jacsau.2c00281
JACS Au 2022, 2, 2001−2012

(43) Han, J.; Du, Z.; Lim, M. H. Mechanistic insight into the design of chemical tools to control multiple pathogenic features in Alzheimer's disease. *Acc. Chem. Res.* **2021**, *54*, 3930−3940.
(44) Atrián-Blasco, E.; Gonzalez, P.; Santoro, A.; Alies, B.; Faller, P.; Hureau, C. Cu and Zn coordination to amyloid peptides: from fascinating chemistry to debated pathological relevance. *Coord. Chem. Rev.* **2018**, *371*, 38−55.
(45) Cao, C.; Cirauqui, N.; Marcaida, M. J.; Buglakova, E.; Duperrex, A.; Radenovic, A.; Dal Peraro, M. Single-molecule sensing of peptides and nucleic acids by engineered aerolysin nanopores. *Nat. Commun.* **2019**, *10*, 4918.
(46) Fuller, C. W.; Kumar, S.; Porel, M.; Chien, M.; Bibillo, A.; Stranges, P. B.; Dorwart, M.; Tao, C.; Li, Z.; Guo, W.; Shi, S.; Korenblum, D.; Trans, A.; Aguirre, A.; Liu, E.; Harada, E. T.; Pollard, J.; Bhat, A.; Cech, C.; Yang, A.; Arnold, C.; Palla, M.; Hovis, J.; Chen, R.; Morozova, I.; Kalachikov, S.; Russo, J. J.; Kasianowicz, J. J.; Davis, R.; Roever, S.; Church, G. M.; Ju, J. Real-time single-molecule electronic DNA sequencing by synthesis using polymer-tagged nucleotides on a nanopore array. *Proc. Natl. Acad. Sci. U. S. A.* **2016**, *113*, 5233−5238.
(47) Frank, M.; Ahrens, J.; Bejenke, I.; Krick, M.; Schwarzer, D.; Clever, G. H. Light-induced charge separation in densely packed donor-acceptor coordination cages. *J. Am. Chem. Soc.* **2016**, *138*, 8279−8287.
(48) Lee, W.; Jung, S.; Kim, M.; Hong, S. Site-selective direct C−H pyridylation of unactivated alkanes by triplet excited anthraquinone. *J. Am. Chem. Soc.* **2021**, *143*, 3003−3012.
(49) Kawaai, K.; Yamaguchi, T.; Yamaguchi, E.; Endo, S.; Tada, N.; Ikari, A.; Itoh, A. Photoinduced generation of acyl radicals from simple aldehydes, access to 3-acyl-4-arylcoumarin derivatives, and evaluation of their antiandrogenic activities. *J. Org. Chem.* **2018**, *83*, 1988−1996.
(50) Yadav, R. K.; Baeg, J.-O.; Oh, G. H.; Park, N.-J.; Kong, K.-J.; Kim, J.; Hwang, D. W.; Biswas, S. K. A photocatalyst-enzyme coupled artificial photosynthesis system for solar energy in production of formic acid from CO_2. *J. Am. Chem. Soc.* **2012**, *134*, 11455−11461.
(51) Reece, S. Y.; Seyedsayamdost, M. R.; Stubbe, J.; Nocera, D. G. Photoactive peptides for light-initiated tyrosyl radical generation and transport into ribonucleotide reductase. *J. Am. Chem. Soc.* **2007**, *129*, 8500−8509.
(52) Ou, H. D.; Phan, S.; Deerinck, T. J.; Thor, A.; Ellisman, M. H.; O'Shea, C. C. ChromEMT: visualizing 3D chromatin structure and compaction in interphase and mitotic cells. *Science* **2017**, *357*, eaag0025.
(53) Chen, G.-f.; Xu, T.-h.; Yan, Y.; Zhou, Y.-r.; Jiang, Y.; Melcher, K.; Xu, H. E. Amyloid beta: structure, biology and structure-based therapeutic development. *Acta. Pharmacol. Sin.* **2017**, *38*, 1205−1235.
(54) Haber, A.; Aviram, M.; Gross, Z. Protecting the beneficial functionality of lipoproteins by 1-Fe, a corrole-based catalytic antioxidant. *Chem. Sci.* **2011**, *2*, 295−302.
(55) Gomes, L. M. F.; Mahammed, A.; Prosser, K. E.; Smith, J. R.; Silverman, M. A.; Walsby, C. J.; Gross, Z.; Storr, T. A catalytic antioxidant for limiting amyloid-beta peptide aggregation and reactive oxygen species generation. *Chem. Sci.* **2019**, *10*, 1634−1643.
(56) Núñez Montoya, S. C.; Comini, L. R.; Sarmiento, M.; Becerra, C.; Albesa, I.; Argüello, G. A.; Cabrera, J. L. Natural anthraquinones probed as Type I and Type II photosensitizers: singlet oxygen and superoxide anion production. *J. Photochem. Photobiol. B* **2005**, *78*, 77−83.
(57) Gollnick, K.; Held, S.; Mártire, D. O.; Braslavsky, S. E. Hydroxyanthraquinones as sensitizers of singlet oxygen reactions: quantum yields of triplet formation and singlet oxygen generation in acetonitrile. *J. Photochem. Photobiol. A* **1992**, *69*, 155−165.
(58) Miliani, C.; Romani, A.; Favaro, G. Acidichromic effects in 1,2-di- and 1,2,4-tri- hydroxyanthraquinones. A spectrophotometric and fluorimetric study. *J. Phys. Org. Chem.* **2000**, *13*, 141−150.
(59) Suzuki, K.; Kobayashi, A.; Kaneko, S.; Takehira, K.; Yoshihara, T.; Ishida, H.; Shiina, Y.; Oishi, S.; Tobita, S. Reevaluation of absolute luminescence quantum yields of standard solutions using a spectrometer with an integrating sphere and a back-thinned CCD detector. *Phys. Chem. Chem. Phys.* **2009**, *11*, 9850−9860.
(60) Wessels, J. M.; Foote, C. S.; Ford, W. E.; Rodgers, M. A. J. Photooxidation of tryptophan: $O_2(^1\Delta_g)$ versus electron-transfer pathway. *Photochem. Photobiol.* **1997**, *65*, 96−102.
(61) Nam, J. S.; Kang, M.-G.; Kang, J.; Park, S.-Y.; Lee, S. J. C.; Kim, H.-T.; Seo, J. K.; Kwon, O.-H.; Lim, M. H.; Rhee, H.W.; Kwon, T.-H. Endoplasmic reticulum-localized iridium(III) complexes as efficient photodynamic therapy agents via protein modifications. *J. Am. Chem. Soc.* **2016**, *138*, 10968−10977.
(62) Son, G.; Lee, B. I.; Chung, Y. J.; Park, C. B. Light-triggered dissociation of self-assembled β-amyloid aggregates into small, nontoxic fragments by ruthenium (II) complex. *Acta Biomater.* **2018**, *67*, 147−155.
(63) Brédas, J.-L.; Beljonne, D.; Coropceanu, V.; Cornil, J. Charge-transfer and energy-transfer processes in π-conjugated oligomers and polymers: a molecular picture. *Chem. Rev.* **2004**, *104*, 4971−5003.
(64) Mohammed, O. F.; Xiao, D.; Batista, V. S.; Nibbering, E. T. J. Excited-state intramolecular hydrogen transfer (ESIHT) of 1,8-dihydroxy-9,10-anthraquinone (DHAQ) characterized by ultrafast electronic and vibrational spectroscopy and computational modeling. *J. Phys. Chem. A* **2014**, *118*, 3090−3099.
(65) Flom, S. R.; Barbara, P. F. Proton transfer and hydrogen bonding in the internal conversion of S_1 anthraquinones. *J. Phys. Chem.* **1985**, *89*, 4489−4494.
(66) Choi, J. R.; Jeoung, S. C.; Cho, D. W. Time-resolved anisotropy study on the excited-state intramolecular proton transfer of 1-hydroxyanthraquinone. *Bull. Korean Chem. Soc.* **2003**, *24*, 1675−1679.
(67) Suess, C. J.; Hirst, J. D.; Besley, N. A. Quantum chemical calculations of tryptophan → heme electron and excitation energy transfer rates in myoglobin. *J. Comput. Chem.* **2017**, *38*, 1495−1502.
(68) Subotnik, J. E.; Vura-Weis, J.; Sodt, A. J.; Ratner, M. A. Predicting accurate electronic excitation transfer rates via Marcus theory with Boys or Edmiston−Ruedenberg localized diabatization. *J. Phys. Chem. A* **2010**, *114*, 8665−8675.
(69) Sherbrook, E. M.; Jung, H.; Cho, D.; Baik, M.-H.; Yoon, T. P. Brønsted acid catalysis of photosensitized cycloadditions. *Chem. Sci.* **2020**, *11*, 856−861.
(70) Pareras, G.; Palusiak, M.; Duran, M.; Solà, M.; Simon, S. Tuning the strength of the resonance-assisted hydrogen bond in *o*-hydroxybenzaldehyde by substitution in the aromatic ring[1]. *J. Phys. Chem. A* **2018**, *122*, 2279−2287.
(71) Latour, V.; Pigot, T.; Simon, M.; Cardy, H.; Lacombe, S. Photo-oxidation of di-*n*-butylsulfide by various electron transfer sensitizers in oxygenated acetonitrile. *Photochem. Photobiol. Sci.* **2005**, *4*, 221−229.
(72) Dhakal, P.; Kuzyk, M. G. Molecular structure and reversible photodegradation in anthraquinone dyes. *J. Photochem. Photobiol. A* **2016**, *328*, 66−76.
(73) Ni, W.; Chen, W.; Lu, Y. Emerging findings into molecular mechanism of brain metastasis. *Cancer Med.* **2018**, *7*, 3820−3833.
(74) Avdeef, A.; Bendels, S.; Di, L.; Faller, B.; Kansy, M.; Sugano, K.; Yamauchi, Y. PAMPA−critical factors for better predictions of absorption. *J. Pharm. Sci.* **2007**, *96*, 2893−2909.
(75) Di, L.; Kerns, E. H.; Fan, K.; McConnell, O. J.; Carter, G. T. High throughput artificial membrane permeability assay for blood−brain barrier. *Eur. J. Med. Chem.* **2003**, *38*, 223−232.
(76) Mormino, E. C.; Kluth, J. T.; Madison, C. M.; Rabinovici, G. D.; Baker, S. L.; Miller, B. L.; Koeppe, R. A.; Mathis, C. A.; Weiner, M. W.; Jagust, W. J.; Alzheimer's Disease Neuroimaging, I.. Episodic memory loss is related to hippocampal-mediated β-amyloid deposition in elderly subjects. *Brain* **2008**, *132*, 1310−1323.
(77) Reilly, J. F.; Games, D.; Rydel, R. E.; Freedman, S.; Schenk, D.; Young, W. G.; Morrison, J. H.; Bloom, F. E. Amyloid deposition in the hippocampus and entorhinal cortex: quantitative analysis of a transgenic mouse model. *Proc. Natl. Acad. Sci. U. S. A.* **2003**, *100*, 4837−4842.
(78) Wengenack, T. M.; Whelan, S.; Curran, G. L.; Duff, K. E.; Poduslo, J. F. Quantitative histological analysis of amyloid deposition

https://doi.org/10.1021/jacsau.2c00281
JACS Au 2022, 2, 2001−2012

in Alzheimer's double transgenic mouse brain. *Neuroscience* **2000**, *101*, 939−944.
(79) Kim, K. S.; Miller, D. L.; Sapienza, V. J.; Chen, C. M. J.; Bai, C.; Grundke-Iqbal, I.; Currie, C. J.; Wisniewski, H. M. Production and characterization of monoclonal antibodies reactive to synthetic cerebrovascular amyloid peptide. *Neurosci. Res. Commun.* **1988**, *2*, 121−130.
(80) Kim, K. S.; Wen, G. Y.; Bancher, C.; Chen, C. M. J.; Sapienza, V. J.; Hong, H.; Wisniewski, H. M. Detection and quantitation of amyloid β-peptide with 2 monoclonal-antibodies. *Neurosci. Res. Commun.* **1990**, *7*, 113−122.
(81) Kayed, R.; Head, E.; Thompson, J. L.; McIntire, T. M.; Milton, S. C.; Cotman, C. W.; Glabe, C. G. Common structure of soluble amyloid oligomers implies common mechanism of pathogenesis. *Science* **2003**, *300*, 486−489.
(82) Kelényi, G. Thioflavin S fluorescent and Congo red anisotropic stainings in the histologic demonstration of amyloid. *Acta Neuropathol.* **1967**, *7*, 336−348.
(83) Urbanc, B.; Cruz, L.; Le, R.; Sanders, J.; Ashe, K. H.; Duff, K.; Stanley, H. E.; Irizarry, M. C.; Hyman, B. T. Neurotoxic effects of thioflavin S-positive amyloid deposits in transgenic mice and Alzheimer's disease. *Proc. Natl. Acad. Sci. U. S. A.* **2002**, *99*, 13990−13995.
(84) Mora, A. K.; Khan, S.; Patro, B. S.; Nath, S. Is DAPI assay of cellular nucleic acid reliable in the presence of protein aggregates? *Chem. Commun.* **2020**, *56*, 13844−13847.
(85) Simard, A. R.; Soulet, D.; Gowing, G.; Julien, J.-P.; Rivest, S. Bone marrow-derived microglia play a critical role in restricting senile plaque formation in Alzheimer's disease. *Neuron* **2006**, *49*, 489−502.
(86) Lee, S. J. C.; Nam, E.; Lee, H. J.; Savelieff, M. G.; Lim, M. H. Towards an understanding of amyloid-β oligomers: characterization, toxicity mechanisms, and inhibitors. *Chem. Soc. Rev.* **2017**, *46*, 310−323.
(87) Benilova, I.; Karran, E.; De Strooper, B. The toxic Aβ oligomer and Alzheimer's disease: an emperor in need of clothes. *Nat. Neurosci.* **2012**, *15*, 349−357.
(88) Lorenzo, A.; Yankner, B. A. Amyloid fibril toxicity in Alzheimer's disease and diabetes. *Ann. N.Y. Acad. Sci.* **1996**, *777*, 89−95.
(89) Tsai, J.; Grutzendler, J.; Duff, K.; Gan, W.-B. Fibrillar amyloid deposition leads to local synaptic abnormalities and breakage of neuronal branches. *Nat. Neurosci.* **2004**, *7*, 1181−1183.
(90) Chen, W.-T.; Lu, A.; Craessaerts, K.; Pavie, B.; Sala Frigerio, C.; Corthout, N.; Qian, X.; Laláková, J.; Kühnemund, M.; Voytyuk, I.; Wolfs, L.; Mancuso, R.; Salta, E.; Balusu, S.; Snellinx, A.; Munck, S.; Jurek, A.; Fernandez Navarro, J.; Saido, T. C.; Huitinga, I.; Lundeberg, J.; Fiers, M.; De Strooper, B. Spatial transcriptomics and in situ sequencing to study Alzheimer's disease. *Cell* **2020**, *182*, 976−991.

https://doi.org/10.1021/jacsau.2c00281
JACS Au 2022, 2, 2001−2012